

S1 Kinetic Inductance in Semiconductor 2DEG and 3D Bulk Metal

S1.1 Kinetic Inductance Derivation Using the Drude Model

Consider a 2D conductor strip of width W and length l . Let a time-dependent voltage $V(t)$ be applied across the length, which yields an electric field $V(t)/l$ along the strip[†]. Newton's law of motion for an electron in the strip, after including the electron scattering effect, yields

$$-e \frac{V}{l} - \frac{m^* v}{\tau} = m^* \frac{dv}{dt}, \quad (\text{S1})$$

which is the Drude model^{S1}. Here m^* is the effective electron mass, τ is the electron scattering time, and v is the electron velocity. In frequency domain, this differential equation translates to

$$-e \frac{V}{l} - \frac{m^* v}{\tau} = m^* i\omega v. \quad (\text{S2})$$

Using current $I = -n_{2D} e v W$, we convert Eq. (S2) to an expression for the 2D strip's impedance¹²,

$$\frac{V}{I} = i\omega \frac{m^*}{n_{2D} e^2} \times \frac{l}{W} + \frac{m^*}{n_{2D} e^2 \tau} \times \frac{l}{W}. \quad (\text{S3})$$

Since an inductive impedance takes the form of $i\omega \times (\text{inductance})$, the first, imaginary term, originating from the acceleration term $m^* dv/dt$ of Eq. (S1), is inductive; the corresponding inductance

[†]In general, the collective electron acceleration along the 2DEG strip considered here, which manifests as kinetic inductance, is part of plasmonic wave excitation along the strip (not to be confused with the effective wave traversing perpendicularly to the strips). But in our work, the plasmonic wavelength is mostly much longer than the strip, obviating the need to consider full plasmonic wave behaviors; we can/do treat the 2D strip as a lumped kinetic inductor¹². This is why no position dependency is assumed for the electric field. See also Sec. S2.2.

is the kinetic inductance due to the collective electron acceleration:

$$L_{k,2D} = \frac{m^*}{n_{2D}e^2} \times \frac{l}{W}. \quad (\text{S4})$$

The second, real term in Eq. (S3), which originates from the scattering term of Eq. (S1), represents the resistance of the 2D conductor strip:

$$R_{2D} = \frac{m^*}{n_{2D}e^2\tau} \times \frac{l}{W} = \frac{1}{n_{2D}e\mu} \times \frac{l}{W}, \quad (\text{S5})$$

where μ is the mobility. Eq. (S3) may then be rewritten as

$$\frac{V}{I} = i\omega L_{k,2D} + R_{2D}. \quad (\text{S6})$$

Thus from the circuit point of view, the 2D conductor strip is the kinetic inductor $L_{k,2D}$ in series with the resistor R_{2D} , and its quality factor is given by

$$Q = \omega \frac{L_{k,2D}}{R_{2D}} = \omega\tau. \quad (\text{S7})$$

In sum, the magnitude of the kinetic inductance $L_{k,2D}$ is given by Eq. (S4) with no dependence on τ , and its impact is *felt* appreciably when $Q = \omega\tau > 1$ (or equivalently, when the inductive impedance is larger than the resistance). In our GaAs/AlGaAs 2DEG, $\tau \sim 0.2$ ns at 4 K, with which the kinetic inductance effect is felt appreciably at and above GHz frequencies. When $Q \ll 1$, the kinetic inductance effect is masked by the electron scattering effects.

The same derivation goes for a 3D conductor with a length l and a cross-sectional area A , leading to the following 3D kinetic inductance and resistance:

$$L_{k,3D} = \frac{m}{n_{3D}e^2} \times \frac{l}{A}, \quad (\text{S8})$$

$$R_{3D} = \frac{m}{n_{3D}e^2\tau} \times \frac{l}{A} = \frac{1}{n_{3D}e\mu} \times \frac{l}{A}. \quad (\text{S9})$$

S1.2 Alternative Kinetic Energy Derivation via Energy Consideration

The kinetic inductance can be alternatively derived from the energy point of view. Using such method, here we re-derive the 2D kinetic inductance of Eq. (S4) for the 2D conductor of width W and length l , where electrons collectively accelerate along the length (x -axis) in response to an electric field. Consider the k -space (while throughout this paper k is reserved for the wavenumber for the effective wave, in this subsection only, k is used as the electron wavenumber). After electrons accelerate towards the positive x -axis for a certain time duration, the 2D Fermi disk (with the diameter of Fermi wavenumber k_F) whose center originally lies at the k -space origin [Fig. S1; Fermi disk **A**] will shift towards the positive k_x -axis by a certain amount Δk [Fig. S1; Fermi disk **B**], thus producing a total current of I . While $\Delta k \ll k_F$, Fig. S1 greatly exaggerates the shift. Our agenda is to calculate the total kinetic energy increase ΔE due to the electrons' collective acceleration, to calculate I , and finally to relate ΔE and I to extract the 2D kinetic inductance.

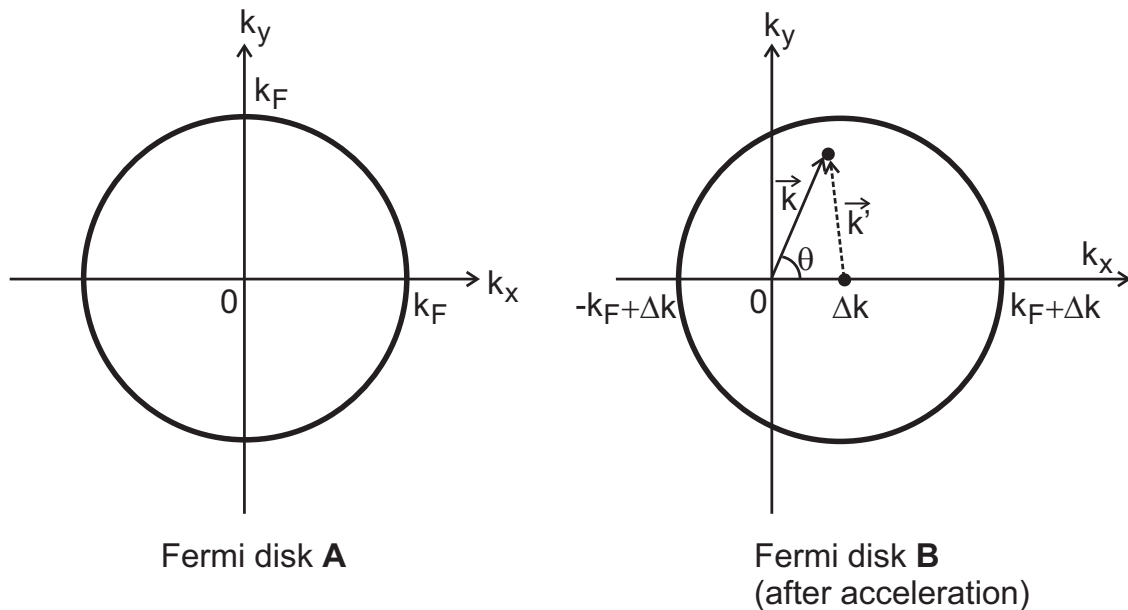


Figure S1: Fermi disks in the k -space.

The total kinetic energy corresponding to the Fermi disk **B** is computed as below, where $\vec{k} = (k_x, k_y)$ and $\vec{k}' = (k'_x, k'_y) = \vec{k} - \Delta k \hat{x}$ (\hat{x} : unit vector along the k_x direction) are with reference to

Fig. S1:

$$\begin{aligned}
E_{\mathbf{B}} &= Wl \iint_{\mathbf{B}} 2 \times \frac{dk_x}{2\pi} \frac{dk_y}{2\pi} \frac{\hbar^2 |\vec{k}|^2}{2m^*} = Wl \times \frac{\hbar^2}{4\pi^2 m^*} \iint_{\mathbf{B}} dk_x dk_y |\vec{k}' + \Delta k \hat{x}|^2 \\
&= Wl \times \frac{\hbar^2}{4\pi^2 m^*} \iint_{\mathbf{B}} dk_x dk_y \left[|\vec{k}'|^2 + 2k'_x \Delta k + (\Delta k)^2 \right]. \tag{S10}
\end{aligned}$$

The last line contains three terms. By inspection of Fig. S1, the first term is simply $E_{\mathbf{A}}$, the total kinetic energy corresponding to the Fermi disk \mathbf{A} . The second term vanishes, due to the odd symmetry of k'_x within the Fermi disk \mathbf{B} . Then Eq. (S10) reduces to

$$\Delta E = E_{\mathbf{B}} - E_{\mathbf{A}} = Wl \times \frac{\hbar^2}{4\pi^2 m^*} (\Delta k)^2 \iint_{\mathbf{B}} dk_x dk_y = Wl \times \frac{\hbar^2 k_F^2}{4\pi m^*} (\Delta k)^2. \tag{S11}$$

The total current I is calculated as

$$\begin{aligned}
I &= W \iint_{\mathbf{B}} 2 \times \frac{dk_x}{2\pi} \frac{dk_y}{2\pi} e \frac{\hbar k_x}{m^*} = W \times \frac{e\hbar}{2\pi^2 m^*} \iint_{\mathbf{B}} dk_x dk_y k_x \\
&= W \times \frac{e\hbar}{2\pi^2 m^*} \int_0^{2\pi} d\theta \cos \theta \int_0^{k_F + \Delta k \cos \theta} k^2 dk. \tag{S12}
\end{aligned}$$

The last line uses the polar coordinate, $k \equiv |\vec{k}|$ and θ , and approximates the distance between the origin and the edge of the Fermi disk \mathbf{B} at angle θ as $k_F + \Delta k \cos \theta$, which is an excellent approximation for $\Delta k \ll k_F$. Performing this integration up to the first order in Δk , we obtain

$$I = W \times \frac{e\hbar}{2\pi m^*} k_F^2 \Delta k. \tag{S13}$$

By eliminating Δk using Eqs. (S11) and (S13), and noting $k_F^2 = 2\pi n_{2D}$, we get

$$\Delta E = \frac{1}{2} \left[\frac{m^*}{n_{2D} e^2} \times \frac{l}{W} \right] I^2. \tag{S14}$$

In analogy to energy of a magnetic inductor with current I being $1/2 \cdot (\text{inductance}) \cdot I^2$, we identify what is in the bracket of Eq. (S14) as the 2D kinetic inductance, which is identical to Eq. (S4).

S1.3 Numerical Comparison of Semiconductor 2DEG Kinetic Inductance and 3D Bulk Metal Kinetic Inductance

Table S1: Kinetic and magnetic inductances per unit length for 3D gold nanoparticles with various cross-sectional areas. L_m is estimated assuming no other conductors nearby.

A	$L_{k,3D}/l$	L_m/l	$L_{k,3D}/L_m$
$1 \times 1 \text{ nm}^2$	600 pH/ μm	$\sim 1.4 \text{ pH}/\mu\text{m}$	430
$5 \times 5 \text{ nm}^2$	24 pH/ μm	$\sim 1.2 \text{ pH}/\mu\text{m}$	20
$10 \times 10 \text{ nm}^2$	6.0 pH/ μm	$\sim 1.0 \text{ pH}/\mu\text{m}$	6
$20 \times 20 \text{ nm}^2$	1.5 pH/ μm	$\sim 0.9 \text{ pH}/\mu\text{m}$	1.7

Table S2: Kinetic and magnetic inductances per unit length for GaAs/AlGaAs 2DEG strips with various cross-sectional widths. L_k is calculated using the material parameters of the 2DEG used in this work. L_m is simulated with the Sonnet electromagnetic field solver, with no other conductors nearby, but inside a $400 \mu\text{m} \times 400 \mu\text{m} \times 1000 \mu\text{m}$ conducting box. Each strip is $400 \mu\text{m}$ long and is connected to the walls at the center of the $400 \mu\text{m} \times 1000 \mu\text{m}$ side walls. The magnetic inductance so simulated is frequency dependent, and the table presents the value averaged over $5 \sim 50 \text{ GHz}$ frequency range. This simulation is conservative, as in our actual device, L_m is even smaller due to neighboring strips (*e.g.*, simulated L_m/l for a $1\text{-}\mu\text{m}$ wide strip in the presence of neighboring strips is $0.44 \text{ pH}/\mu\text{m}$, as stated in the main text, instead of $1.4 \text{ pH}/\mu\text{m}$).

W	$L_{k,2D}/l$	L_m/l	$L_{k,2D}/L_m$
20 nm	62.5 nH/ μm	$\sim 2.3 \text{ pH}/\mu\text{m}$	27,000
100 nm	12.5 nH/ μm	$\sim 2.0 \text{ pH}/\mu\text{m}$	6,300
500 nm	2.50 nH/ μm	$\sim 1.6 \text{ pH}/\mu\text{m}$	1,600
1000 nm	1.25 nH/ μm	$\sim 1.4 \text{ pH}/\mu\text{m}$	890

The kinetic inductance, which is the manifestation of the collective electron acceleration, is significantly more pronounced in semiconductor 2DEG than in 3D bulk metal. This is seen from numerical calculations in Tables S1 and S2, where the kinetic and magnetic inductances, L_k and L_m , are calculated for 3D gold nanoparticles¹³ of varying cross-sectional area and for 2DEG strips of varying cross-sectional width. As can be seen, the 2DEG strip has both much larger absolute kinetic inductance and much larger kinetic-to-magnetic inductance ratio. In both quantities, typical cases compare with a factor of at least 100 or more, even when the 2DEG strip has much larger cross-sectional linear scale than the 3D gold nanoparticle. For the same cross-sectional linear scale ($\sqrt{A} = W$), the difference is even larger (*e.g.*, one can compare the bottom row of Table S1 to the top row of Table S2 where $\sqrt{A} = W = 20 \text{ nm}$; L_k/l is a factor of 42,000 larger, and L_k/L_m

is a factor of 16,000 larger). Note that the kinetic-to-magnetic inductance ratio is a key factor determining the magnitude of the negative index, thus, these tables show the impact of creating a large negative index by utilizing the 2DEG kinetic inductance.

S2 Dispersion Relation

S2.1 Derivation

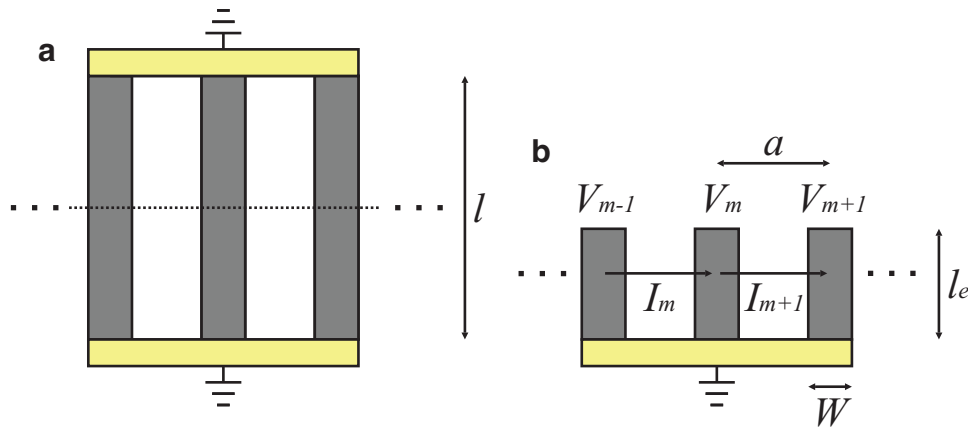


Figure S2: **a**, 2DEG strip array. Dark regions indicate 2DEG. **b**, Half-structure cut at the horizontal symmetry line. Only the effective length l_e of each 2DEG strip is relevant.

This section derives the dispersion relation for the *effective wave* traveling through the 2DEG strip array (Fig. S1a). Since no current flows *vertically* through the center of any strip due to symmetry, only the lower/upper half below/above the horizontal symmetry line can be considered (Fig. S2b). In this half-structure, each strip has width W , effective length[‡] l_e , and periodicity a . Each strip in this half-structure may be considered as a lumped kinetic inductance $L_{k,2D}$ of Eq. (S4), with l replaced with l_e in the equation. We ignore the loss for simplicity. The interactions between two neighboring strips within the effective length can be modeled using a lumped capacitance C

[‡]Because the field distribution of the guided modes in the CPWs is concentrated between the signal and ground lines, not the total geometric strip length l but the effective length l_e within which the guided modes accelerate electrons is relevant. To a good approximation, the distance between the signal and ground lines of the CPWs can be used for l_e , as shown in Fig. 2b, right.

between them (we only consider the nearest-neighbor couplings for simplicity), given by^{S2}

$$C = \epsilon l_e \frac{K(\sqrt{1-u^2})}{K(u)}, \quad (\text{S15})$$

where $u \equiv (a - W) / (a + W)$, ϵ is the effective, averaged permittivity of the surroundings, and $K(u)$ is the complete elliptic integral of the first kind:

$$K(u) = \int_0^{\pi/2} \frac{d\theta}{\sqrt{1-u^2 \sin^2 \theta}}. \quad (\text{S16})$$

C does not vary simply with the inter-strip distance, $a - W$, but varies in a more complicated fashion with u , due to the confinement into two dimensions. The strip array then can be thought of as a capacitively-coupled inductor array [Fig. S3]. This lumped circuit model is a good approximation, for the plasmonic wavelength along the strip is mostly much longer than the strip [Sec. S2.2].

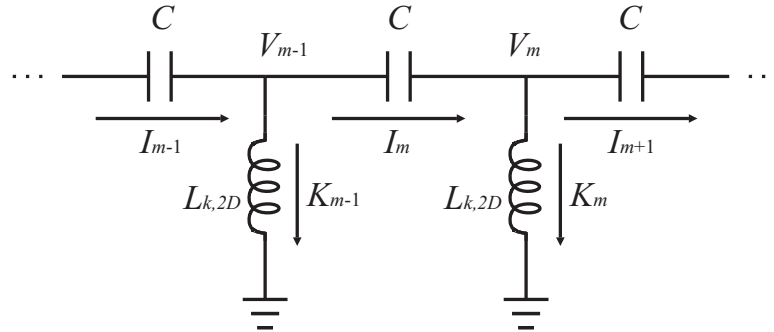


Figure S3: Circuit model for the 2DEG strip array.

The effective wave is represented by voltage $\{\dots, V_{m-1}, V_m, V_{m+1}, \dots\}$ at the tips of the kinetic inductors [Figs. S2 and S3]. For the m -th capacitor's current, we have:

$$C \frac{d}{dt} (V_{m-1} - V_m) = I_m. \quad (\text{S17})$$

According to the Kirchhoff's current law, we have

$$I_m - I_{m+1} = K_m, \quad (\text{S18})$$

where K_m is the current flowing through the m -th kinetic inductor, and is related to V_m via

$$V_m = L_{k,2D} \frac{dK_m}{dt}. \quad (\text{S19})$$

By combining Eqs. (S17), (S18), and (S19), we obtain the following wave equation:

$$\frac{1}{L_{k,2D}C} V_m = \frac{d^2}{dt^2} (V_{m-1} + V_{m+1} - 2V_m). \quad (\text{S20})$$

Plugging $V_m = V_0 e^{i(\omega t - kma)}$ into Eq. (S20), where k is the effective wavenumber and ω is the angular frequency, we obtain the following dispersion relation:

$$\omega(k) = \frac{1}{2\sqrt{L_{k,2D}C}} \left| \sin \frac{ka}{2} \right|^{-1} = \omega_c \left| \sin \frac{ka}{2} \right|^{-1}, \quad (\text{S21})$$

where

$$\omega_c \equiv \frac{1}{2\sqrt{L_{k,2D}C}} \quad (\text{S22})$$

is the cutoff frequency corresponding to $k = \pm\pi/a$, the first Brillouin-zone boundary. Eq. (S21) exhibits opposite signs of $d\omega/dk$ and ω/k (group and phase velocities) for $\omega > \omega_c$, showing negative refraction. This holds for both $k > 0$ and $k < 0$, but in Fig. 2a, we only show $k < 0$, as $k > 0$ is irrelevant to the measurements of this work (Secs. S3.2 and S5). The refractive index is in general[§]

$$n = \frac{\text{sgn}(d\omega/dk)}{\text{sgn}(\omega/k)} \times |k|c/\omega, \quad (\text{S23})$$

where $\text{sgn}(x) \equiv x/|x|$. By using Eq. (S21) here, we obtain:

$$n = -\frac{2c}{a\omega} \sin^{-1} \left(\frac{\omega_c}{\omega} \right). \quad (\text{S24})$$

[§]In our measurements (Secs. S3.2 and S5), if the device under test is negatively [positively] refracting, $k < 0$ [$k > 0$], so the index expression reduces to $n = kc/\omega$.

S2.2 Plasmonic Wave Consideration

So far we have represented the effect of the collective electron acceleration along the 2DEG strip as a lumped kinetic inductor. More generally, this collective electron acceleration is part of the collective plasmonic wave excitation *along* the 2DEG strip¹² (not to be confused with the effective wave traversing *perpendicularly* to the strips). Plasmonic waves are created when the equilibrium electron density distribution is disturbed; Coulomb forces and electron degeneracy pressure arise to bring the electron density distribution back to equilibrium, which powers plasmonic waves, accelerating electrons collectively, yielding time-varying kinetic energy of these electrons. Another defining energetic component of the plasmonic wave is the time-varying potential energy due to the Coulomb interaction and degeneracy pressure. The plasmonic wave's dispersion relation can be calculated^{18,S3} by using the Lindhard dielectric function obtained within the random phase approximation framework^{S4}. This dispersion relation depends on the presence/absence and proximity of grounded conducting objects (*e.g.*, top gate) in the environment, as they influence the detailed Coulomb interactions within the 2DEG.

The plasmonic wave behaviors within an individual 2DEG strip can be understood from the circuit point of view, by treating the strip as a 'plasmonic transmission line,' which is a ladder network of distributed kinetic inductances and distributed capacitances^{12,S5,S6}. The distributed kinetic inductances account for the time-varying kinetic energy (acceleration) of electrons; the kinetic inductance per unit length is given by $L' \equiv L_{k,2D}/l$ from Eq. (S4). The distributed capacitances with the per-unit-length value of C' account for the time-varying potential energy due to the Coulomb interaction and degeneracy pressure within the 2DEG strip; in our frequency range, the degeneracy pressure effect is negligible, and C' is of purely electrostatic nature. These distributed capacitances C' in the plasmonic line are connected to ground at their one end, and should not be confused with the inter-strip capacitance C of Eq. (S15) that plays a role in propagating the effective wave through the strip array. C' is generally frequency dependent, and depends on the presence/absence and detailed configuration of grounded conducting objects nearby. The plasmonic velocity is $v_p = 1/\sqrt{L'C'}$, which is equivalent to the aforementioned plasmonic dispersion obtained through the Lindhard dielectric function in the limiting case of negligible degeneracy pressure. The

plasmonic line's characteristic impedance is $Z_0 = \sqrt{L'/C'}$.

As discussed shortly, in our work, the plasmonic wavelength, λ_p , along the strip is mostly much longer than the strip's effective length l_e , or equivalently $k_p l_e \ll 1$ (k_p : plasmonic wavenumber). In this long wavelength regime, our 2DEG plasmonic line, whose one end is grounded via finite ohmic contact resistance R_c that is much smaller than Z_0 , acts as a lumped kinetic inductor¹². This can be seen by calculating the input impedance Z_{in} of the 2DEG strip at its non-grounded end. To begin with, with $R_c \ll Z_0$, we have^{S7}

$$Z_{in} = Z_0 \frac{R_c + iZ_0 \tan k_p l_e}{Z_0 + iR_c \tan k_p l_e} \approx iZ_0 \tan k_p l_e. \quad (\text{S25})$$

Now with $k_p l_e \ll 1$, $\tan k_p l_e \sim k_p l_e$, thus, Z_{in} further reduces to

$$Z_{in} \approx iZ_0 k_p l_e = iZ_0 \frac{\omega}{v_p} l_e = i\omega L' l_e. \quad (\text{S26})$$

This shows that the 2DEG strip behaves as a lumped kinetic inductor $L' l_e$, which is no more than $L_{k,2D}$ of Eq. (S4) with l replaced with l_e . In fact, even when a longer wavelength is considered without satisfying $k_p l_e \ll 1$, as far as $k_p l_e < \pi/2$, Z_{in} is still inductive with the inductance value even larger than $L' l_e$, as seen from Eq. (S25), thus, the strip array will maintain negative refraction. By contrast, if $k_p l_e > \pi/2$, Z_{in} would become capacitive, making negative refraction vanish in the strip array device. In between these two regimes, *i.e.*, at $k_p l_e = \pi/2$ ($l_e = \lambda_p/4$), plasmonic standing wave resonance occurs.

To compare λ_p to l_e in our frequency range, we get a feel for λ_p by resorting to Stern's ungated 2D plasmonic dispersion relation¹⁸

$$\omega = \sqrt{\frac{k_p n_{2D} e^2}{2\epsilon m^*}}, \quad (\text{S27})$$

where $n_{2D} = 1.9 \times 10^{11}/\text{cm}^2$, $m^* = 0.067m_e$, and ϵ is the effective permittivity given by $\epsilon = \kappa_{\text{effective}}\epsilon_0$, with $\kappa_{\text{effective}} = (\kappa_{\text{GaAs}} + \kappa_{\text{Air}})/2 = 6.95$, in which we safely ignore the very thin AlGaAs layer (71 nm, including a thin GaAs cap)^{S8}. Let us consider the longest strip ($l = 112 \mu\text{m}$; $l_e = 31 \mu\text{m}$) employed in this work. At 50 GHz, $\lambda_p \sim 400 \mu\text{m} \sim 3.6l \sim 13l_e$; at 25 GHz,

$\lambda_p \sim 1600 \mu\text{m} \sim 14l \sim 50l_e$. So even at 50 GHz and even with the longest strip, $k_p l_e \sim 0.5$ and $\tan(k_p l_e) \sim 0.54 \sim k_p l_e$; thus, even in this conservative case, Eq. (S26) is valid, justifying the treatment of the 2DEG as a lumped kinetic inductance given by Eq. (S4) with l replaced by l_e . The first plasmonic standing wave resonance condition $l_e = \lambda_p/4$ is beyond our frequency range. To be even more conservative (albeit not realistic), even with the actual geometric length l , the first plasmonic standing wave condition $l = \lambda_p/2$ is still beyond our frequency range.

S2.3 Dependency of n on $L_{k,2D}$

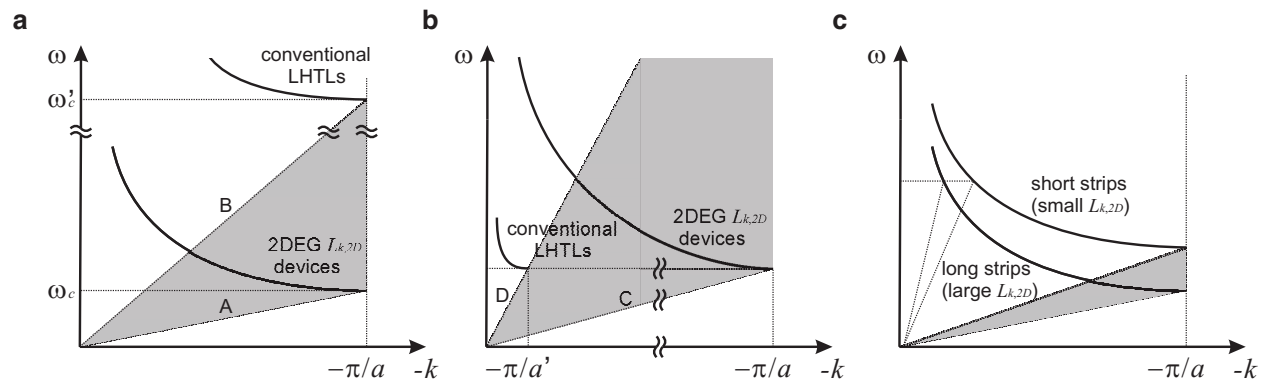


Figure S4: **a**, Comparison of the dispersion relations for conventional left-handed transmission lines (LHTLs) and our 2DEG strip array metamaterials for the same a . **b**, Comparison of the dispersion relations for conventional LHTLs and our 2DEG strip array metamaterials for the same ω_c . **c**, Comparison of our metamaterials with shorter and longer strips for the same a . Plots are not drawn to scale.

With Eqs. (S21) and (S24), we examine how the very large $L_{k,2D}$ yields the extraordinarily strong negative refraction, in comparison to the conventional left-handed transmission line¹⁵⁻¹⁷, which has essentially the same dispersion expression, but with magnetic inductance L_m in the place of $L_{k,2D}$. Imagine a left-handed transmission line with similar physical dimensions to our 2DEG strip array. For example, one can think of the same strip array as our metamaterial with the same geometric parameters (a , W , and l), but with L_m replacing $L_{k,2D}$. Since this left-handed line and our metamaterial have the same l , $L_{k,2D} \gg L_m$. For example, $L_{k,2D}$ is $1.25 \text{ nH}/\mu\text{m}$ for a $1\text{-}\mu\text{m}$ wide 2DEG strip, which is 2,800 times larger than the same strip's L_m , $0.44 \text{ pH}/\mu\text{m}$. In this case, the left-handed line's cutoff frequency ω'_c is far larger than our metamaterial's cutoff frequency ω_c [Eq. (S22)], while a remains the same. Their dispersion relations are illustrated in Fig. S4a. The

slope of a straight line connecting the origin and a (ω, k) point is the phase velocity ω/k at frequency ω . Entering the shaded region forbidden for the left-handed line, our metamaterial achieves a range of ω/k values far smaller than the minimum ω/k of the left-handed line. Equivalently, in this region, our metamaterial exhibits a range of negative refractive index values much larger in magnitude than the maximum negative index of the left-handed line. The largest attainable negative index for our metamaterial (which corresponds to line **A**, Fig. S4a), $n = -2c/(a\omega_c)$, is much larger in magnitude than that for the left-handed line (line **B**), $n = -2c/(a\omega'_c)$, as $\omega_c \ll \omega'_c$.

Alternatively, one can consider a left-handed line and our metamaterial with $L_m = L_{k,2D}$; since the magnetic inductance per unit length is much smaller than the kinetic inductance per unit length, $L_m = L_{k,2D}$ will mandate much larger physical dimensions for the magnetic inductors. In this scenario, ω_c can be made the same between our metamaterial and the left-handed line, but due to the much larger physical dimensions of the magnetic inductors, the left-handed line's periodicity a' will be much larger than our metamaterial's periodicity a . The dispersion relations for these two devices are illustrated in Fig. S4b. In the shaded area forbidden for the left-handed line, our metamaterial exhibits a range of negative refractive index values much larger in magnitude than the maximum negative index of the left-handed line. The largest attainable negative index for our metamaterial (line **C** in Fig. S4b) $n = -2c/(a\omega_c)$ is much larger in magnitude than that for the left-handed line (line **D** in Fig. S4b) $n = -2c/(a'\omega_c)$, as $a' \gg a$.

In measurements of Figs. 4a-b of the main text, for the same a and W , l is increased from 52 μm to 112 μm , increasing C and $L_{k,2D}$, thus decreasing ω_c . The resulting index change in Figs. 4a-b, which was explained algebraically in the main text, can be understood graphically as well. Fig. S4c shows the dispersion curves for our metamaterial with the same a but differing ω_c . Only the longer-strip metamaterial can access the shaded region, in which it attains negative indices larger in magnitude than the maximum negative index of the shorter-strip metamaterial; the longer-strip metamaterial has a larger maximum attainable negative refractive index. On the other hand, at the same frequency accessible for both metamaterials, the shorter-strip metamaterial exhibits a larger negative refractive index. These clear-cut properties are evident in Figs. 4a-b of the main text.

S2.4 Frequency Scaling

Measurements in Fig. 4 of the main text show, in keeping with the theory, that reducing the strip length l increases ω_c , but reduces $|n|$, and this $|n|$ -reduction can be offset by decreasing the periodicity a . In fact, it is feasible to increase ω_c while maintaining a similar range of $|n|$, by reducing both l and a in a particular fashion, which we discuss now using the maximum attainable refractive index magnitude, $|n_{max}| \equiv 2c/(a\omega_c)$.

If l is reduced by a factor of* α (< 1), and a and W are reduced by a factor of β (< 1), ω_c is altered by a factor of $\sqrt{\beta}/\alpha$ [Eqs. (S4), (S15), and (S22)] and $|n_{max}|$ is changed by a factor of $\alpha/\beta^{3/2}$. To keep $|n_{max}|$ constant, we must have $\alpha = \beta^{3/2}$; ω_c will then increase by a factor of $1/\beta = \alpha^{-2/3}$. As our 13-strip metamaterial with $l = 112 \mu\text{m}$, $W = 1 \mu\text{m}$, and $a = 1.25 \mu\text{m}$ has a cutoff frequency of ~ 10 GHz, to scale up the cutoff frequency to 1 THz while keeping $|n_{max}|$, $\beta = 1/100$ and $\alpha = 1/1000$. Thus this THz device would have $l = 112$ nm, $W = 10$ nm, and $a = 12.5$ nm. These W and a dimensions are at the verge of what is feasible with the current top-down fabrication technologies. In going to the 1-THz device, if we allow $|n_{max}|$ to reduce by a factor of 5 (with which $|n_{max}|$ is still ~ 100), $\beta = 0.05$ and $\alpha = 0.00224$, yielding $l = 251$ nm, $W = 50$ nm, and $a = 62.5$ nm, which are well within the capability of current top-down fabrication technologies.

This high-frequency scaling is a theoretical projection; actual implementation of such small devices is expected to face various challenges. For example, the edge depletion effect, which is not a significant issue in the current work, will become pronounced when the 2DEG strip becomes narrower, as the edge depletion portion becomes an increasingly significant fraction of the strip, thus mandating careful design considerations. Coupling of the THz electromagnetic waves into such small negative refraction devices can pose another challenge, which one may be able to overcome by using wide-band log periodic antennae or other forms of electromagnetic structures^{S9}. At the same time, the small structures might offer some interesting avenues to explore. For example, as the 2DEG strip width approaches tens of nanometers, the 2DEG would start exhibiting 1D quantum wire behaviors (especially if it is operated at low temperatures, although the main text suggests the

*To be rigorous, one must consider the scaling of l_e , but here we seek to provide the essence simply.

high-frequency scaling as a means to potentially achieve the room temperature operation), with 1D kinetic inductance quantized per each conduction channel. Exploiting this 1D kinetic inductance, if observable, for negative refraction would offer an interesting opportunity.

High-mobility graphene^{S10}, which was suggested in the main text as another 2D conductor platform where similar metamaterials can be possibly built, would have similar dimensions and scaling properties as our GaAs 2DEG devices, because graphene's kinetic inductance with a feasible doping density is expected to be a few hundred pH/square^{S6}, which is on the same order of magnitude as the kinetic inductance used in this work.

S3 Calibration, De-embedding, and Extraction of n

S3.1 Calibration and De-embedding

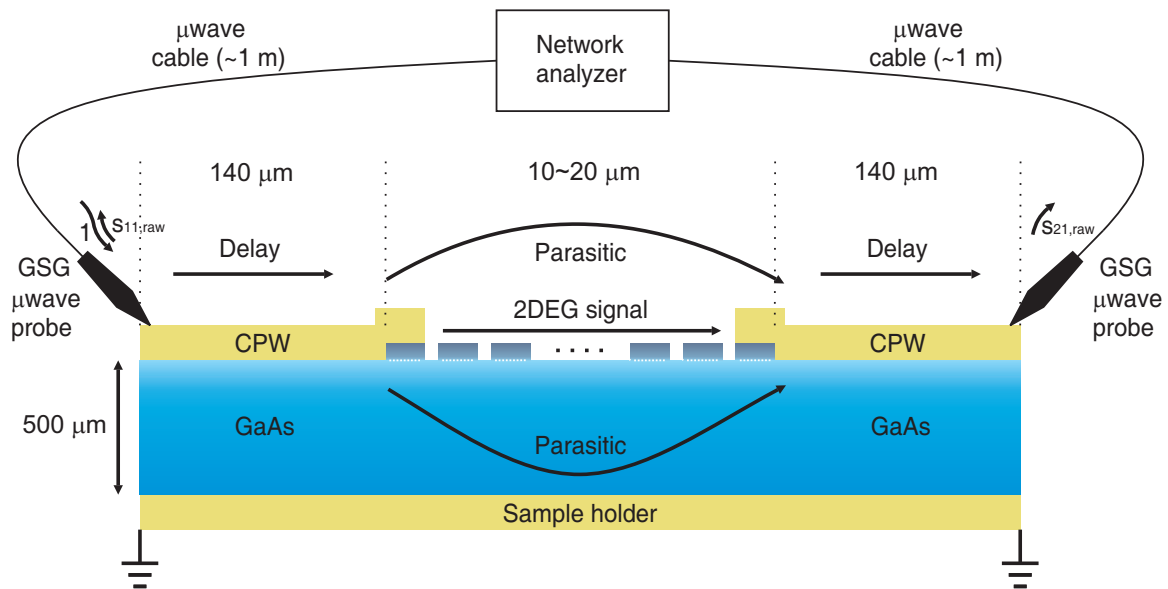


Figure S5: Schematic showing the vertical cross section of the measured device, the measurement setup, and the constituent signal components.

Fig. S5 schematically shows the vertical cross section of the device and the measurement setup. The raw s -parameters, $s_{11,raw}$ and $s_{21,raw}$, shown in the figure are obtained at the probe tips after calibrating out the effects of the cables and probes. These raw s -parameters still contain the

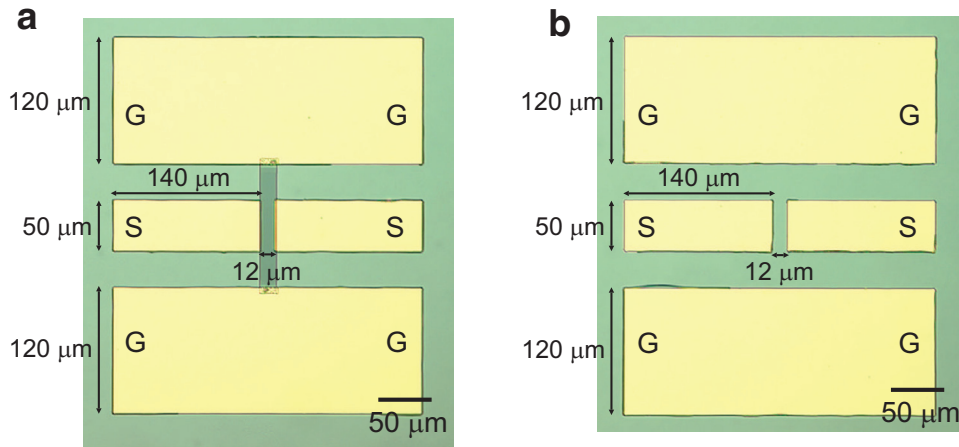


Figure S6: **a**, Optical image of the $a = 1.25 \mu\text{m}$, $l = 112 \mu\text{m}$ device of Fig. 4, with CPWs of length $140 \mu\text{m}$ to the left and right of the strip array. **b**, The same CPWs fabricated on a separate undoped GaAs substrate without the strip array. This ‘open’ device is used for measuring the parasitic coupling between the two CPWs.

propagation effects on the on-chip CPWs that lead from the probes to the strip array device as well as the parasitic couplings between the two CPWs which bypass the strip array, in addition to the actual response of the strip array. Therefore, to see the pure effect of the 2DEG strip array only, we de-embed these on-chip CPW propagation effects and their parasitic couplings. We explain below how the system is first calibrated up to the probe tips to attain the raw s -parameters, and how the on-chip CPW propagation effects and their parasitic couplings are de-embedded. All calibrations and de-embedding measurements are performed at the same temperature as the corresponding actual device measurements.

For the calibration up to the probe tips, we use the NIST-style multi-line TRL technique²⁹, which entails s -parameter measurements of a separate set of CPWs of varying lengths and load configurations. This separate calibration substrate fabricated on an undoped GaAs substrate³⁰ matches the conditions of the actual metamaterial chips, for the CPWs on the metamaterial devices lie over the regions where the donor layers and 2DEG are removed by etching³⁰.

We de-embed the propagation effects of the CPWs (mostly phase delay with negligible losses) using a standard calibration feature in the calibration software (Cascade Microtech WinCal XE), which calculates the transmission matrix of the CPWs of desired length (*e.g.*, $140 \mu\text{m}$ for the device in Fig. S6a) and de-embeds it. After this step, the s -parameters now reflect the desired 2DEG device

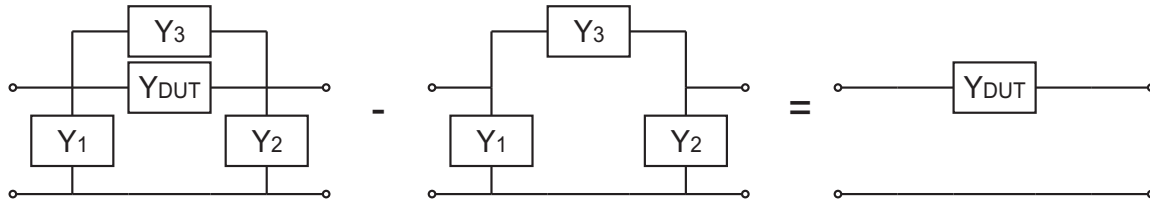


Figure S7: Illustration of the parasitic coupling de-embedding method. The method de-embeds the direct parasitic coupling between the signal lines (Y_3) as well as the parasitic couplings to the ground (Y_1 , Y_2), so that only the responses of the metamaterial device under test (DUT) are left.

response and the parasitic couplings between the two on-chip CPWs. To de-embed these parasitic couplings, we fabricate and measure a device with identical CPWs but without the 2DEG strips (e.g., Fig. S6b). De-embedding is performed by first converting the s -parameters measured from the actual device (e.g., Fig. S6a) and the ‘open’ device (e.g., Fig. S6b) into corresponding sets of y -parameters, subtracting the open device y -parameters from the actual device y -parameters, and converting the resultant y -parameters back to s -parameters^{S11} (Fig. S7). This step finally leads to the bona fide s -parameters that reflect the pure effect of the 2DEG device.

S3.2 Extraction of n

From this final set of s_{21} and s_{11} parameters at each measurement frequency, we extract the effective wavenumber k inside the metamaterial, by using the standard prescription detailed in Refs. 19 and 20. Specifically, k is given by:[¶]

$$e^{ikd} = X \pm i\sqrt{1 - X^2},$$

$$X = \frac{1 - s_{11}^2 + s_{21}^2}{2s_{21}}. \quad (\text{S28})$$

Due to causality and analyticity, k can be uniquely determined despite the apparent multiplicity of signs and branches^{19,20}. This extraction connects the s_{21} and s_{11} parameters at any given measurement frequency f to the wavenumber k at the same frequency, thus, leading to the f - k dispersion curve, such as Fig. 3a. The measured s_{21} and s_{11} parameters set the left-to-right energy

[¶]These formulas directly from Refs. 19 and 20 use the phasor convention of $e^{i(kz - \omega t)}$, which differs from the phasor convention $e^{i(\omega t - kz)}$ our vector network analyzer uses. For the extraction to be consistent with our phasor convention, we actually use s_{11}^* and s_{21}^* in these formulas, which leads to exactly the same physical results^{S12}.

propagation direction (*i.e.*, group velocity direction) as the positive reference direction. Therefore, if the device under test is negatively [positively] refracting, the extracted k 's sign will be minus [plus], with no arbitrariness. For any physically meaningful situation, the refraction sign decision based on the sign of the extracted k will be consistent with the refraction sign decision made by examining the extracted dispersion curve as to whether the $d\omega/dk$ tangential slope (group velocity) and ω/k slope (phase velocity) have the opposite or same signs. In sum, a negative [positive] refraction device will yield a negative [positive] k in our setup, and consistently, opposite [same] signs for $d\omega/dk$ and ω/k . In Fig. 3a, $d\omega/dk$ and ω/k have opposite signs in the bright region, and the sign of k is minus, both of which consistently confirm negative refraction in the bright region. From the dispersion relation in the bright region, the negative refractive index is obtained by $n = kc/\omega$.

In the dark region of Fig. 3a of the main text where the cutoff behavior occurs and the de-embedded $|s_{21}|$ becomes exceedingly small mostly below^{||} -30 dB, the extraction method above becomes increasingly error-prone, as discussed in Ref. 19 and as can be seen from Eq. (S28). This can result in a dispersion relation which is physically not meaningful or mathematically troublesome without being able to satisfy the causality condition¹⁹. For example, in the dark region of Fig. 3a, the group velocity is negative, while the energy actually propagates in the positive reference direction, which is a contradiction; an alternative way of viewing this contradiction is that in the dark region, $k < 0$ indicates negative refraction, but the identical signs of $d\omega/dk$ and ω/k suggest positive refraction. Thus, calculating n is meaningless with its sign indeterminable in this cutoff region, and we truncate the effective index curves in cutoff regions in the main text. However, we show the dispersion in the dark region in Fig. 3a to use the spurious behavior as an indicator of the cutoff region.

^{||}Note that this is smaller than what is shown in Fig. 3d, which is the s_{21} magnitude before de-embedding the parasitic signals.

S4 Additional Data

S4.1 Pre-De-Embedding Dispersion and Index

Fig. S8 corresponds to Figs. 3a-c of the main text, but without the parasitic coupling de-embedded; as mentioned in the main text, Figs. 3a-c are obtained after the full de-embedding. By comparing Figs. 3a-c and Fig. S8, we see that the positively refracting parasitic coupling lowers the magnitude of the measured negative index, as expected. Even when the parasitic coupling is treated as a part of the device response, the measured effective index is still very large on the order of hundreds (Fig. S8b). The parasitic coupling is also seen to lower the measured loss and cause the figure of merit to be overestimated (Fig. 3c vs. Fig. S8c).

S4.2 Full s -parameter Data

Fig. S9 shows the entire set of the raw s -parameter data up to the probe tips for the device of Fig. 3 of the main text; in the main text, only the magnitudes of s_{11} and s_{21} were presented due to space constraints. Each set of data, now including phase information, clearly shows that the 2DEG device behaves largely consistently as a negative index metamaterial at temperatures of 4.2 K, 10 K, and 20 K, while its behavior is completely different at 297 K. This once again confirms the negative refraction due to kinetic inductance in the acceleration-dominated regime (4.2 K, 10 K, and 20 K) and the open-circuit behavior in the scattering-dominated regime (297 K). In addition, all of these data show that the 2DEG device's behavior at 297 K much resembles the behavior of the device having only the CPWs with no 2DEG strip array (labeled 'open' in Fig. S9); this once again attests to the open-circuit behavior of the metamaterial at 297 K, with the kinetic inductance completely masked by electron scattering.

S5 Comparison to Positively Refracting Structures

To further illuminate our negative refraction strategy in contrast to positive refraction and also to check the soundness of our methods for calibration, de-embedding, and effective index extraction (albeit well established and broadly used), we have fabricated and measured positively refracting

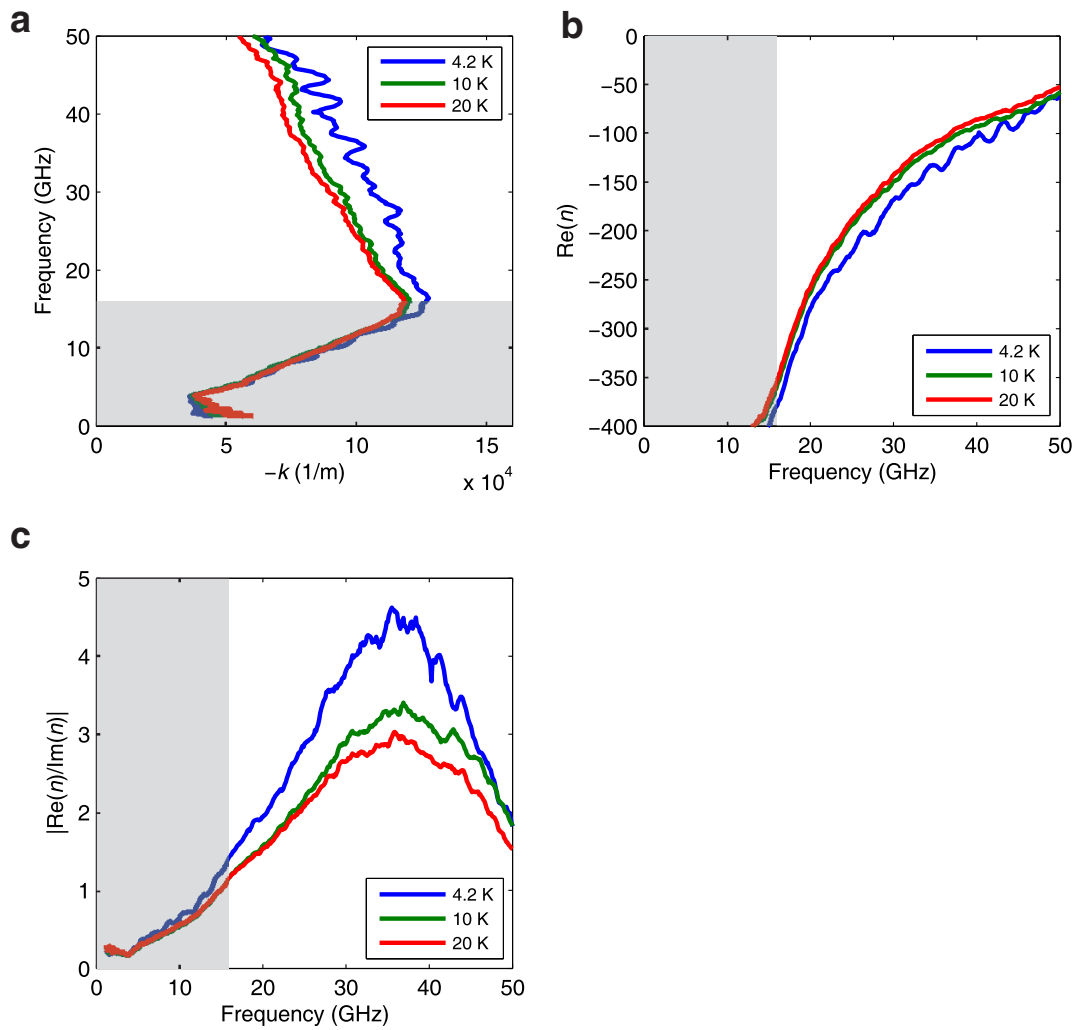


Figure S8: Measurement results of the device of Fig. 3, without the parasitic coupling de-embedded. Panels a, b, and c correspond to Figs. 3a-c.

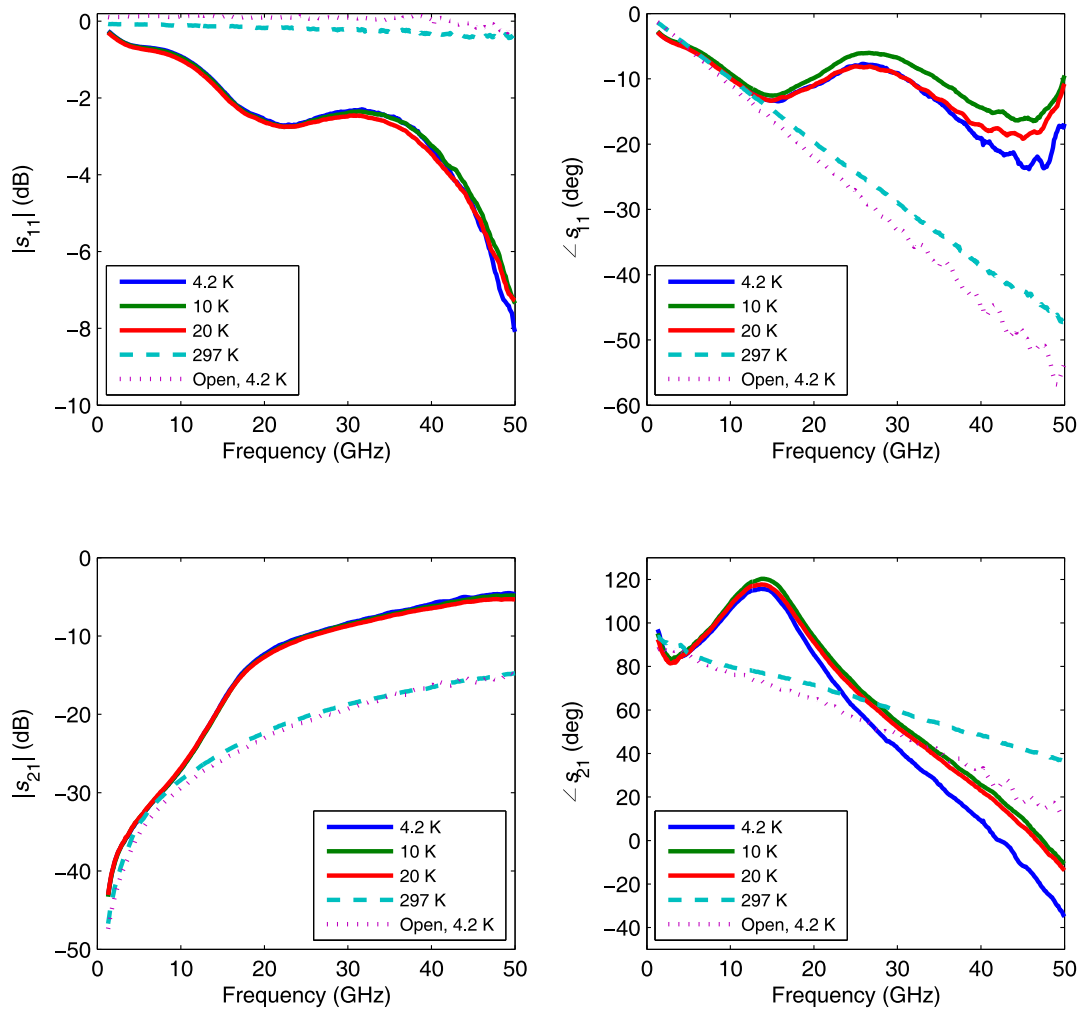


Figure S9: Full s -parameter data for the device of Fig. 3. $|s_{11}|$ is slightly (~ 0.1 dB; 2 %) larger than 0 dB for the 'open' device measurement, due to the calibration error.

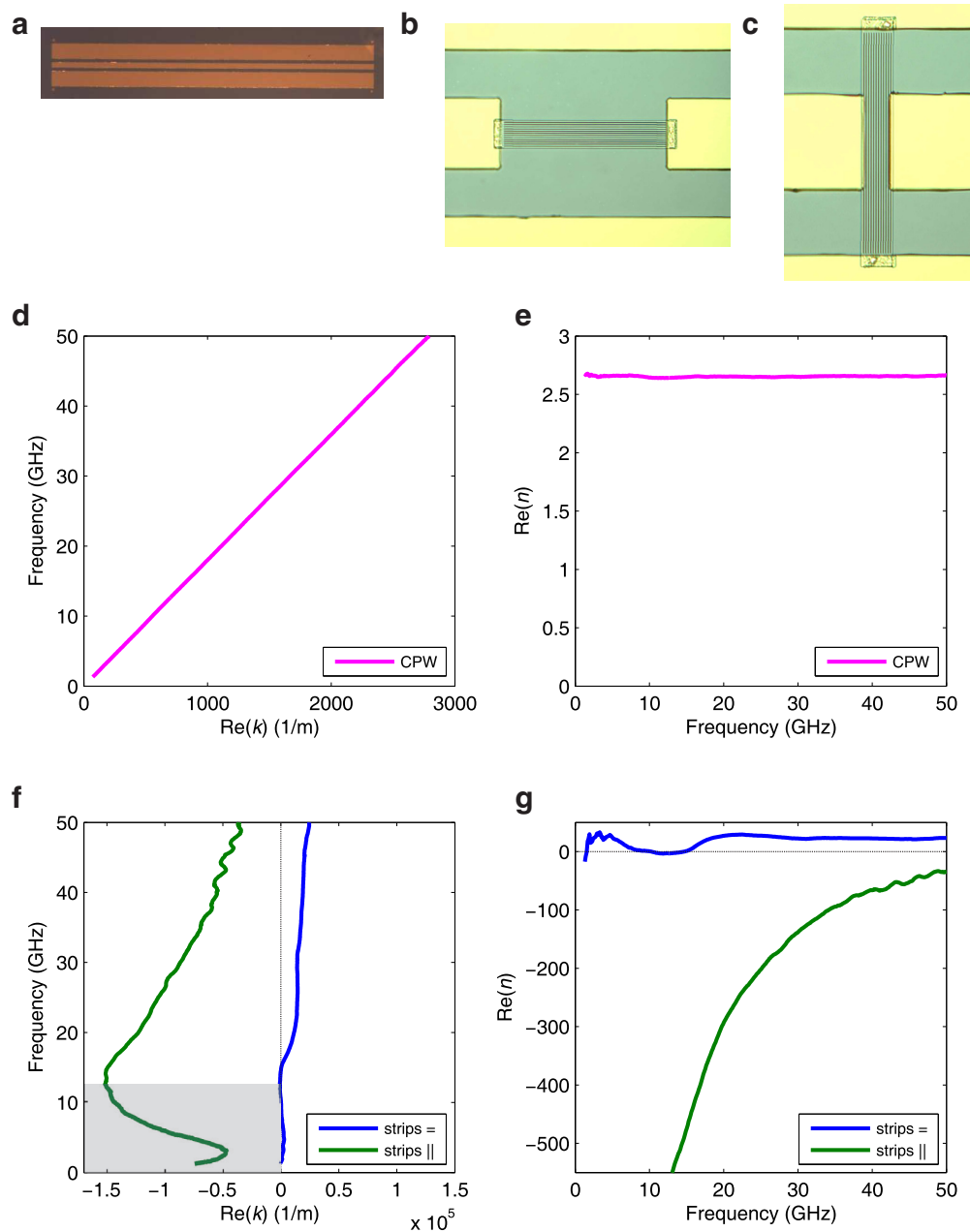


Figure S10: Comparison of dispersion relations and effective refractive indices for positively refracting and negatively refracting structures. **a**, 3-mm CPW on GaAs (CPW). **b**, 2DEG strip array excited *along* the direction of the strips (strips =). **c**, The negative index metamaterial device of Fig. 3 reshown here to facilitate the comparison (strips ||). **d,e**, Measured dispersion and effective refractive index, respectively, for the device of **a**. **f,g**, Measured dispersions and effective refractive indices, respectively, for the devices of **b** and **c**. All measurements were performed at 4.2 K.

structures. All measurements, calibration, de-embedding (if applicable), and effective index extraction procedures performed on these structures are exactly the same as those used for our negative index metamaterials. As discussed in Sec. S3.2, because in all of our measurements the measured s_{21} and s_{11} parameters set the left-to-right energy propagation direction (*i.e.*, group velocity direction) as the positive reference direction, if the device under test is positively [negatively] refracting, the extracted k 's sign will be plus [minus] with no ambiguity, and at the same time, $d\omega/dk$ and ω/k will have the same [opposite] signs. Fig. S10 juxtaposes the measurement results of our metamaterial device of Fig. 3 with the measurement results of these positively refracting devices.

Fig. S10a shows a 3-mm long electromagnetic coplanar waveguide (CPW) on a GaAs substrate. Its measured dispersion relation (Fig. S10d) shows the same signs for $d\omega/dk$ and ω/k , and consistently with this, k is positive, thus, the CPW is positively refracting, as is well known. The effective dielectric constant $\kappa_{\text{effective}}$ of ~ 7 for this CPW is the average of the dielectric constants of GaAs and air. This leads to an effective refractive index of $n = \sqrt{\kappa_{\text{effective}}} = 2.64$. This is matched by the measured index (Fig. S10e).

Fig. S10b shows the same 2DEG strip array as the device measured for Fig. 3 ($a = 1.25 \mu\text{m}$, $W = 1.0 \mu\text{m}$, and $l = 112 \mu\text{m}$), but with excitation *along* the strips. We expect positive refraction; in fact, as all strips are excited together, this device does not feel the inter-strip capacitances, thus, is more or less the same as a *sheet* of 2DEG. The measured dispersion indeed shows the positive refraction, consistently judged by $k > 0$, and by the same signs of $d\omega/dk$ and ω/k (Fig. S10f, blue). The refractive index extracted from measurements is ~ 23 in a good part of the measurement frequency range (Fig. S10g, blue), with the lower frequency regions showing fluctuations due to low $|s_{21}|$, where impedance mismatch and losses are severe. The index of this device is larger than that of the electromagnetic CPW, because the former comes from the plasmonic excitation (in the long plasmonic wavelength regime), or equivalently, as it involves collective electron accelerations. The index ~ 23 of this device, however, is not as large in magnitude as the negative index of our metamaterial, because the inter-strip capacitance does not participate in the dynamics in the former.

Finally, Fig. S10c shows our negative index metamaterial measured for Fig. 3. Its measured

dispersion and index (Figs. 3a-b of the main text) are repeated here (Figs. S10f-g, green) to facilitate the comparison with the positive refraction devices. In the main text, the dispersion relation was plotted with $-k$ as the x -axis. Here, we use k as the x -axis. Of course, the data are exactly identical (in either case, $k < 0$). Both the negative sign of k and the opposite signs of $d\omega/dk$ and ω/k in the measured dispersion in the bright region consistently confirm negative refraction. Contrast from the positive refraction devices is evident.

S6 Simulation Setup

Fig. 2b was simulated using the Sonnet frequency-domain electromagnetic field solver. For a conductor, the simulator takes a complex resistivity as a simulation parameter; we use the real part of the resistivity to model the electron scattering effect in the 2DEG, and its imaginary part to model the kinetic inductance of the 2DEG.

The simulated structure lies in a $400 \mu\text{m} \times 400 \mu\text{m} \times 1000 \mu\text{m}$ (x , y , and z) box surrounded by conducting side and bottom walls. Inside the box there are three dielectric layers; from bottom up, the first layer is $500 \mu\text{m}$ -thick GaAs with $\kappa_{\text{GaAs}} = 12.9$ (which corresponds to the actual thickness of the GaAs substrate below the 2DEG), the second layer is 71 nm -thick AlGaAs with $\kappa_{\text{AlGaAs}} = 12.9$ (which corresponds to the actual thickness of the AlGaAs and GaAs cap above the 2DEG), and the third layer is $500 \mu\text{m}$ thick air with $\kappa_{\text{Air}}=1.0$. Between the first and second dielectric layers lies the 2DEG structure; the 2DEG's resistance per square 7.2Ω and kinetic inductance per square 1.25 nH are entered into the aforementioned complex resistivity parameter. Between the second and third dielectric layers, we define the gold CPWs with conductivity $4.09 \times 10^7 \text{ S/m}$ and thickness $0.5 \mu\text{m}$ (which corresponds to the actual thickness of the CPWs). In the actual structure, most parts of the CPWs sit directly on top of GaAs, instead of AlGaAs as defined in the simulation, as most of AlGaAs except where the 2DEG strips are defined is etched away. However, this makes only a negligible difference as the 71-nm thickness of the AlGaAs layer is much smaller than the relevant wavelengths.

The 2DEG is formed into strips of width $1 \mu\text{m}$ and length $112 \mu\text{m}$, separated from each other with $0.25 \mu\text{m}$ gaps (*i.e.*, periodicity is $1.25 \mu\text{m}$). There are a total of 13 strips in the strip array.

The ohmic contact between each 2DEG strip and the CPWs' ground is modeled as a $1\ \mu\text{m} \times 1\ \mu\text{m}$ conductor (at the 2DEG layer level) with a resistance of $450\ \Omega/\text{square}$, which is an estimation (the real contact resistance varies from device to device); the ohmic contact is completed by inserting a resistance-less vertical via to the gold CPW layer.

CPWs are designed to possess a $50\text{-}\Omega$ characteristic impedance on air-clad GaAs substrate. The dimensions of the CPWs are signal line width $50\ \mu\text{m}$, gaps between the signal line and the ground lines $32\ \mu\text{m}$, and ground line width $143\ \mu\text{m}$ (top and bottom). In the real devices, slightly narrower ($120\ \mu\text{m}$) ground lines were used due to space constraints on the small 2DEG samples, but this causes only a negligible change in the characteristic impedance of the CPWs, and the measured signal as well, as confirmed by additional simulations and experiments. The signal lines extend over the first two 2DEG strips from both sides (left and right) of the strip array.

References

- [S1] Ashcroft, N. W. & Mermin, N. D. *Solid State Physics* (Brooks Cole, 1976).
- [S2] Binns, K. J. & Lawrenson, P. J. *Analysis and Computation of Electric and Magnetic Field Problems* (Pergamon Press, 1973).
- [S3] Eguiluz, A., Lee, T. K., Quinn, J. J. & Chiu, K. W. Interface excitations in metal-insulator-semiconductor structures. *Phys. Rev. B* **11**, 4989–4993 (1975).
- [S4] Ehrenreich, H. & Cohen, M. H. Self-consistent field approach to the many-electron problem. *Phys. Rev.* **115**, 786–790 (1959).
- [S5] Staffaroni, M., Conway, J., Vedantam, S., Tang, J. & Yablonovitch, E. Circuit analysis in metal-optics. *arXiv:1006.3126* (2010).
- [S6] Rana, F. Graphene terahertz plasmon oscillators. *IEEE Trans. Nanotech.* **7**, 91–99 (2008).
- [S7] Pozar, D. M. *Microwave Engineering* (Wiley, 2005), 3rd edn.
- [S8] Kukushkin, I. V. *et al.* Observation of retardation effects in the spectrum of two-dimensional plasmons. *Phys. Rev. Lett.* **90**, 156801 (2003).
- [S9] Shaner, E. A. & Lyon, S. A. Time-resolved impulse response of the magnetoplasmon resonance in a two-dimensional electron gas. *Phys. Rev. B* **66**, 041402 (2002).
- [S10] Dean, C. R. *et al.* Boron nitride substrates for high-quality graphene electronics. *Nature Nanotech.* **5**, 722–726 (2010).
- [S11] Aktas, A. & Ismail, M. Pad de-embedding in RF CMOS. *IEEE Circuits Devices Mag.* **17**, 8–11 (2001).
- [S12] Ramakrishna, S. A. Physics of negative refractive index materials. *Rep. Prog. Phys.* **68**, 449–521 (2005).